An Extended Greenwood-Williamson Model Based Normal Interaction Law for Discrete Element Modelling of Spherical Particles with Surface Roughness

T. Zhao, Y. T. Feng*, Min Wang
Zienkiewicz Centre for Computational Engineering, Swansea University, UK

Abstract

The current work aims to develop an improved random normal interaction law based on an extended Greenwood-Williamson (GW) model for spherical particles with surface roughness in the discrete element modelling (DEM) of particle systems. The extended GW model overcomes some theoretical defects of the classic GW model when incorporated into the discrete element framework. Based on two non-dimensional forms in which only two surface roughness parameters are involved, an empirical formula of the improved interaction law is derived by the curve-fitting technique. The resulting interaction law is incorporated into DEM to investigate the mechanical response of particle systems with different surface roughness. Numerical simulations are performed to model one-dimensional and three-dimensional compression tests to explore the macro and micro characteristics of granular particles with surface roughness. The results show that surface roughness makes the initial packing of a particle assembly looser and has a greater influence on looser packed samples as expected, but an assembly with moderate roughness may exhibit a higher strength. The limitations of the current development are also highlighted.

KEYWORDS: Surface roughness; Extended GW model; Normal contact interaction law; Stochastic discrete element modelling; Compression test

1 Introduction

Since it was originated in the 1970s by the pioneer work of Cundall and Strack [1], the discrete element method (DEM) has emerged as a reliable and effective numerical technique to model many scientific and engineering problems involving granular matters and discontinuous materials. The computational framework of the classic DEM is essentially deterministic, in which the material and geometric properties and the loading conditions are assumed to be known *in prior*. The results obtained from a deterministic analysis are implicitly assumed to represent all the possible scenarios of the system. This is, however, not true for most practical problems where a certain degree of uncertainties is always involved, and therefore the traditional deterministic approach may not be able to treat real problems adequately. One deterministic DEM simulation result can only be regarded as one realisation in the context of Monte Carlo simulations. Considering the influence of inherent uncertainties on particulate systems leads to a stochastic discrete element modelling (SDEM) methodology as firstly developed for rough spherical particles in our previous work [2].

*Corresponding author; e-mail: y.feng@swansea.ac.uk

To investigate the response of particle systems, the classic DEM has a disadvantage in simulating complicated shaped objects. Real particles contain geometric irregularities at both macroscopic and microscopic levels. However, basic elements commonly used in DEM are regular geometric entities such as disc, ellipse, ellipsoid and polygon. The surfaces of all the elements are assumed to be smooth. Issues related to geometric uncertainty and its influence on the mechanical behaviour of the particulate system are gaining an increasing attention[3, 4]. In addition to representing complicated shapes by bonding or clumping together several basic entities [5, 6, 7, 8, 9], there has been a continuous effort in DEM to introduce non-spherical entities such as polygons, polyhedra, super-quadrics, and cylinders etc.[11, 12, 13, 14, 15, 16]. Note that such solutions for modelling irregularities of real particles are mostly focused on the macroscopic level.

The geometric irregularities at the microscopic level, also called the surface roughness, are more difficult to be accounted for. The surface roughness can be considered by an interaction law which estimates contact forces between particles. This issue is commonly treated by the tangential contact model involving friction. Moreover, the surface roughness will affect the rolling behaviour of particles, and this issue has been considered in the rotational resistance model [10, 17, 18]. However, these methods treat the surface roughness in a deterministic way, which is not surprising as currently used normal contact laws in DEM, such as the linear and the Hertz contact models, are intended for contact between smooth particles.

A few investigations have been made to develop contact models for rough particles but based on some strong assumptions. By making the idealisation that the contact width is homogeneously distributed with a finite number of normal/tangential basic elements, Jiang et al.[19] develop a two-dimensional roughness theory which introduces two artificial parameters to represent the particle roughness. Wilson et al.[20] derive an analytical model by assuming that the rough particles make contact at exactly 2 points in 2D and 3 points in 3D.

Yet, very few attempts have been reported to address the problem of geometric irregularities in randomness. It may be significant if surface roughness can be included in contact interaction laws in a statistic sense. A first attempt has been made towards this goal in our previous work [2] where a novel random normal interaction law has been proposed.

Our new normal interaction law that considers surface roughness for spheres is based on the classic Greenwood-Williamson (GW) model [21, 22]. As the theoretical basis of this stochastic approach, the GW model plays a crucial role in determining the accuracy and rationality of the resulting interaction model. However, it is found [2] that some theoretical defects may exist when incorporating the classic GW model into DEM simulations and could lead to some unreasonable results. To resolve these issues, an extended GW model is developed in [23]. The main objective of the current work is to derive an improved normal interaction law based on this extended GW model for spherical particles with surface roughness and to incorporated it into DEM.

The paper is organised as follows. Both the classic and the extended GW models are briefly described in the next section. Two non-dimensional forms of the extended GW model are introduced in Section 3. Based on the numerical results, an improved normal interaction law is derived by a two-step curve-fitting method in Section 4. The new interaction law, which can now be incorporated into DEM, is used to investigate the mechanical response of granular assemblies with different roughness parameters in Section 5, where numerical simulations are performed to model one-dimensional and three-dimensional compression tests on granular assemblies, and macro and micro properties of the numerical samples are analysed to investigate the influence of surface roughness on the particle systems. Some concluding remarks are made in Section 6 to highlight the limitations of the current model.

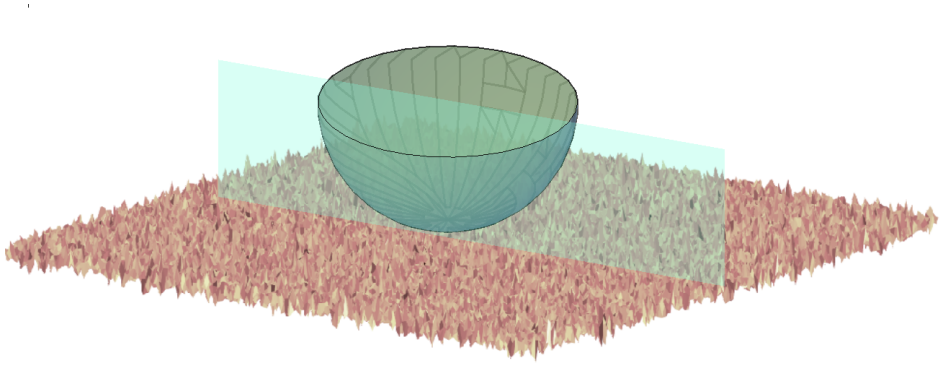

Figure 1: Contact between a smooth sphere and a nominally flat rough surface

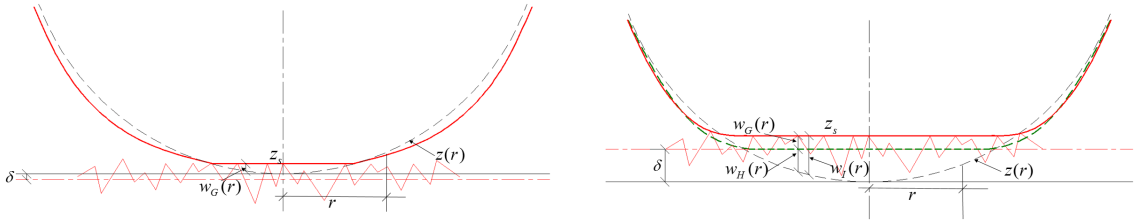

(a) (b)

Figure 2: Profile of the contact between smooth sphere and rough surface based on the classic GW model (a); and the extended GW model (b)

2 The GW model and its Extension

In this section, the classic GW model is briefly reviewed first and then its extension to general contact cases is described which forms the basis for the development of an improved normal contact law in the subsequent sections.

2.1 The classic GW model

A rough surface consists of a myriad of asperities or peaks that restrict the real contact area. Due to the complexity of a rough surface, an appropriate mathematical expression is needed to model a real surface as a profile with asperities that their heights obey a particular statistical distribution, for instance, the Gaussian distribution. This statistical approach to mathematically representing rough surfaces is adopted in the GW model. By further combining with the Hertz theory, a solution to the contact problem of rough surfaces is derived. The elaborated explanation of the GW model can be found in the original work [21, 24] or other related work [2, 22, 25].

The contact between two rough spheres can be mathematically transformed into the contact between a deformable smooth sphere and a nominal rigid flat rough surface as shown in Figure 1. The equivalent radius R and the equivalent standard deviation of the asperity height distribution σ can be obtained by the radii and roughness parameters of the two spheres as

$$\frac{1}{R} = \frac{1}{R_1} + \frac{1}{R_2}; \quad \sigma^2 = \sigma_1^2 + \sigma_2^2 \tag{1}$$

in which subscripts 1 and 2 indicate the sphere number.

Referring to Figure 2(a), δ is the *separation* or *overlap* between the non-deformed configuration of the sphere and the mean line of the flat surface. To make it compatible with the convention of the DEM, δ is assumed to be negative when the two surfaces are in separation, and positive in overlap. $w_{_G}$ is the bulk deformation of the sphere. The profile of the undeformed sphere (black dashed line) can be described by

$$z(r) = \delta - \frac{r^2}{2R} \tag{2}$$

where r is the distance from the centre to the contact point. The overlap of the asperity of height z_s at r with the un-deformed sphere is

$$\delta(r) = z_s - w_{_G}(r) \tag{3}$$

When $\delta(r) > 0$, the contact force between the sphere and the asperity can be computed by the Hertzian theory

$$f(z_s) = \frac{3}{4} E \beta^{1/2} [z_s - w_{_G}(r)]^{3/2} \tag{4}$$

in which β is the radius of the top of the asperity and is assumed to be the same for all the asperities. Further assume that the distribution of the asperity heights obeys the following Gaussian probability density function

$$\phi(z_s) = \frac{1}{\sqrt{2\pi\sigma^2}} \exp\big(-\frac{z_s^2}{2\sigma^2}\big) \tag{5}$$

The probability of having a contact at any given asperity of height z_s is

$$\text{prob}(z_s > w_{_G}(r)) = \int_{w_{_G}(r)}^{+\infty} \phi(z_s) dz_s \tag{6}$$

Then the contact pressure distribution between the sphere and the asperities over the entire contact area can be expressed as

$$p_{_G}(r) = C \int_{w_{_G}(r)}^{+\infty} \big[z_s - w_{_G}(r)\big]^{3/2} \phi(z_s) dz_s \tag{7}$$

with the constant

$$C = \frac{4}{3} E N \beta^{1/2} \tag{8}$$

in which E is the equivalent Young's modulus of the original two spheres, and N is the number of summits in the nominal area. The corresponding deformation $w_{_G}(r)$ can be obtained from the solution to the axi-symmetric deformation of an elastic half-space as follows [28]

$$w_{_G}(r) = \frac{4}{\pi E} \int_0^{\bar{a}} \frac{t}{r+t}\, p_{_G}(t)\, \mathbf{K}(k) dt \tag{9}$$

where $\mathbf{K}(k)$ is the complete elliptic integral of first kind with elliptic modulus

$$k = \frac{2\sqrt{rt}}{r+t} \tag{10}$$

and $\bar{a}$ is the radius of the contact area. By integrating the pressure distribution over the contact area, the total contact force $P_{_G}$ between the sphere and the rough surface with overlap δ can be obtained by

$$P_{_G}(\delta, \sigma) = \int_0^{\bar{a}} 2\pi r\, p_{_G}(r)\, dr \tag{11}$$

The relevant numerical procedure in order to effectively and accurately obtain $P_G(\delta, \sigma)$ has been extensively discussed in [2].

This model contains three roughness parameters N, β and σ which are not easily measurable but may be identified by Nayak's analysis [26] of correlated random fields. The pioneering work in statistical geometry of the oceanographer can be applied to the analysis of surface roughness[27]. Then the parameters of the GW model can be related to the properties of peaks in a two-dimensional, isotropic, Gaussian random field by

$$N = \frac{m_4}{6\pi\sqrt{3}m_2} = \frac{\sqrt{3}}{6\pi l_c^2} \tag{12}$$

$$\beta = \frac{8}{3}\sqrt{\frac{m_4}{\pi}} = \frac{8\sigma_z}{\sqrt{3\pi}l_c^2} \tag{13}$$

$$\sigma = m_0 - \frac{0.8969 m_2^2}{m_4} = 0.7011\sigma_z^2 \tag{14}$$

where l_c and σ_z are the parameters of the random field; and m_0, m_2 and m_4 are the zeroth, second and fourth moments of the power spectral density which is derived from Fourier transform of the surface profile.

2.2 An extended GW model

The classic GW model has been validated (mainly qualitatively though), extended and applied to many applications, see for instance [24, 28, 29, 30, 32]. It is evident, however, that the GW model is better suited for lightly loaded contacts with large separations where the surface asperities deform elastically. Also, the purely elastic model (GW model) overestimates the separation at a given load [30]. This coincides with our previous work, in which a simple extension of the GW model to the case $\delta > 0$ is made but when δ is small, a detailed analysis conducted leads to the following conclusion

$$P_G(\delta) < P_H(\delta) \tag{15}$$

where $P_H(\delta) = \frac{4}{3}E\sqrt{R}\delta^{3/2}$ is the Hertzian contact force for the smooth spheres. Clearly this is not physical as the contact force for the two rough spheres cannot be smaller than the smooth case for the same nominal overlap δ.

The classic GW model has been extended to consider the plastic deformation of the surface asperities under the condition of high loads and small separations. Several plastic models have been proposed in which the deformation is divided into different regimes: elastic, elasto/plastic and fully plastic [29, 30, 31]. In all these models, the inception of the plastic deformation needs to be determined by introducing additional parameters, such as plastic index (or hardness), which are material dependent. As our current work is a preliminary study of developing the random contact law for rough particles contacts in DEM simulation, the classic GW model is used for its simplicity.

To overcome the above mentioned defect of the classic GW model when applied to the DEM simulation, an extended contact model is developed in the current work [23], and briefly introduced as follows.

The rough (flat) surface is divided into two parts: the nominal smooth surface and the rough asperities above, and both parts additively contribute to the deformation of the (smooth) sphere and the final contact force. As shown in the Figure 2(b), the profile in green represents

the deformed sphere in contact only with the smooth surface (i.e. the Hertizan part); while the profile in red represents the final deformed configuration of the sphere in contact with the rough surface.

The contact force due to the smooth part can be obtained from the Hertz law and the additional contact force caused by the asperities is determined by the classic GW model. The contact pressure distribution is the sum of the Hertz pressure distribution in terms of the overlap δ and the GW pressure distribution in terms of the roughness parameter σ.

Thus the total pressure distribution $p_I(r)$ and deformation distribution $w_I(r)$ of the sphere can be expressed by

$$p_I(r) = p_H(r) + p_G(r) \tag{16}$$

$$w_I(r) = w_H(r) + w_G(r) \tag{17}$$

where $p_G(r)$ and $w_G(r)$ are defined by (7) and (9) respectively in the classic GW model; while $p_H(r)$ and $w_H(r)$ are defined by the Hertizan theory with $a_H = \sqrt{R\delta}$ as:

$$p_H(r) = \begin{cases} 0; & r \le a_H \\ \dfrac{2E}{\pi}\dfrac{a_H}{R}\left(1 - \dfrac{r^2}{a_H^2}\right)^{1/2}; & r > a_H \end{cases} \tag{18}$$

$$w_H(r) = \begin{cases} \delta - \dfrac{r^2}{2R}; & r \le a_H \\ \dfrac{a_H^2}{\pi R}\left[\dfrac{r^2}{a_H^2} - 1 + \left(2 - \dfrac{r^2}{a_H^2}\right)\sin^{-1}\left(\dfrac{a_H}{r}\right)\right]; & r > a_H \end{cases} \tag{19}$$

The total contact force $P_I(\delta, \sigma)$ is the summation of the Hertz force $P_H(\delta)$ and the rough GW contribution $P_G(\delta, \sigma)$ defined by (11) as

$$P_I(\delta, \sigma) = P_H(\delta) + P_G(\delta, \sigma) \tag{20}$$

By utilising the fact that the Hertz contribution is zero when δ is negative, the above extended GW model includes the classic case as a special case. For the rough part, p_G can be set to be zero when $\delta < -3\sigma$ because the probability that a summit z_s lies in the range $[-3\sigma, +3\sigma]$ is 99.9%. The comparison with the classic GW model and further discussions of this extended model can be found in [23].

Compared with conventional contact models for smooth spheres such as the linear contact model, and the Hertz contact model, the current contact model explicitly takes account of the influence of sphere roughness on normal contact forces. Also, compared with the other two contact models [19, 20] for rough spheres mentioned in Introduction, which essentially treat the surface roughness in a deterministic way, our contact model considers the random feature of the surface roughness in a statistical sense.

3 Non-dimensional forms

The aim of this work is to establish a normal contact law that can be readily used in DEM. Considering the complicity of the above extended GW model, non-dimensional analysis is performed to make the final formula with a minimum number of parameters. There are three roughness parameters in the GW model: N, β and σ. A non-dimensional parameter, μ, is defined in [24] as

$$\mu = \frac{8}{3}\sigma N\sqrt{2R\beta} \tag{21}$$

$N\beta^{1/2}$ in (11) can be replaced by

$$N\beta^{1/2} = \frac{3\mu}{8\sqrt{2R}\sigma} \tag{22}$$

Then the coefficient C defined by (8) can be expressed in terms of only two roughness parameters σ and μ as

$$C = \frac{3\mu}{8\sqrt{2R}\sigma} \tag{23}$$

The explicit expression between the overlap δ and the total contact force P_I needs to be established following the numerical procedure developed in [2]. To reduce the computational costs and improve the accuracy of the subsequent curve fitted empirical formulas, two non-dimensional forms are presented below using δ and σ as the scaling factor respectively.

Table 1: The scaling factors in two non-dimensional forms

q^*	σ-form	δ-form
δ^*	σ	-
σ^*	-	δ
$w^*_{I/G/H}$	σ	δ
z^*_s	σ	δ
$\phi^*(z^*_s)$	$1/\sigma$	$1/\delta$
r^*	$\sqrt{2R\sigma}$	$\sqrt{2R\delta}$
$\bar{a}^*$	$\sqrt{2R\sigma}$	$\sqrt{2R\delta}$
$p^*_{I/G/H}$	$E\sqrt{\sigma/8R}$	$E\sqrt{\delta/8R}$
$P^*_{I/G/H}$	$P_H(\sigma)$	$P_H(\delta)$

There are three input parameters δ, σ and μ. To reduce the input parameters, two non-dimensional parameters α and α' are defined as

$$\alpha = \frac{\sigma}{\delta}; \quad \alpha' = \frac{1}{\alpha} = \frac{\delta}{\sigma} \tag{24}$$

Table 3 lists the scaling factors for those quantities in the two non-dimensional forms. The non-dimensional expressions of the functions $p_I(r), w_I(r)$ and P_I for the two forms in terms of the non-dimensional parameters α (or α') are presented below.

The δ-form:

$$\begin{aligned} p^*_I(r^*,\alpha) &= p^*_H(r^*) + p^*_G(r^*,\alpha) \\ &= \frac{2a^*}{\pi}\Big(1 - \frac{r^{*2}}{a^{*2}}\Big)^{1/2} + \mu\int_{w^*_G(r^*,\alpha)}^{\infty}\Big[z^*_s - w^*_G(r^*,\alpha)\Big]^{3/2}\phi(z^*_s)dz^*_s \end{aligned} \tag{25}$$

$$\begin{aligned} w^*_G(r^*,\alpha) &= w^*_H(r^*) + w^*_G(r^*,\alpha) \\ &= \Big(1 - \frac{r^{*2}}{2a^{*2}}\Big) + \frac{2}{\pi}\int_0^{\bar{a}^*}\frac{t^*}{t^*+r^*}p^*_G(t^*,\alpha)\mathbf{K}(k)dt^* \end{aligned} \tag{26}$$

$$P^*_I(\alpha,\mu) = P^*_H + P^*_G(\alpha,\mu) = 1 + \frac{3\sqrt{2}}{8}\int_0^{\bar{a}^*} 2\pi r^* p^*_G(r^*,\alpha) \tag{27}$$

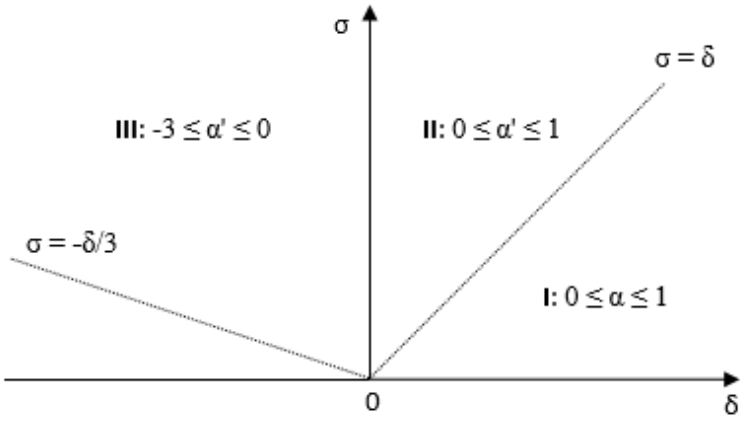

Figure 3: The division of the $\delta - \sigma$ plane into three cases

The σ-form:

$$\begin{aligned} p_I^*(r^*, \alpha') &= p_H^*(r^*) + p_G^*(r^*, \alpha') \\ &= \frac{2a^*}{\pi}\Big(1 - \frac{r^{*2}}{a^{*2}}\Big)^{1/2} + \mu \int_{w_G^*(r^*,\alpha')}^{\infty} \Big[z_s^* - w_G^*(r^*, \alpha')\Big]^{3/2} \phi(z_s^*) dz_s^* \end{aligned} \tag{28}$$

$$\begin{aligned} w_I^*(r^*, \alpha') &= w_H^*(r^*, \alpha') + w_G^*(r^*, \alpha') \\ &= \alpha'\Big(1 - \frac{r^{*2}}{2a^{*2}}\Big) + \frac{2}{\pi}\int_0^{\bar{a}^*} \frac{t^*}{t^* + r^*} p_G^*(t^*, \alpha') \mathbf{K}(k) dt^* \end{aligned} \tag{29}$$

$$P_I^*(\alpha', \mu) = P_H^*(\alpha') + P_G^*(\alpha', \mu) = 1 + \frac{3\sqrt{2}}{8}\int_0^{\bar{a}^*} 2\pi r^* p_G^*(r^*, \alpha') dr^* \tag{30}$$

The total contact force between two rough spheres can be expressed as

$$P_I(\delta, \sigma) = P_H(\delta) P_I^*(\alpha, \mu) = P_H(\sigma) P_I^*(\alpha', \mu) \tag{31}$$

where both non-dimensional coefficients $P_I^*(\alpha, \mu)$ and $P_I^*(\alpha', \mu)$ will be derived in empirical form in the next section.

4 A normal interaction law based on the extended GW model

Interaction laws commonly used in DEM are an explicit formula in terms of the overlap and other parameters of contact features which is obviously different from the extended GW model in (31). Due to the complicity and implicit nature of the extended GW model which cannot be implemented directly into the DEM framework, a curve-fitting procedure is conducted to obtain a normal interaction law based on numerical results. The detailed numerical procedures and computational issues have been discussed in our previous work [2].

As P_H and P_I^* have been separated in (31), only P_I^* needs to be curve-fitted. Moreover, to avoid numerical difficulties, the range of the input parameters has been divided into three parts: Case I: $0 \le \alpha \le 1$; Case II: $0 \le \alpha' \le 1$; and Case III: $-3 \le \alpha' \le 0$, as shown in Figure 3.

Three explicit approximations to P_I^* for the three cases, denoted as $P_{I1}^*(\alpha,\mu)$, $P_{I2}^*(\alpha',\mu)$, $P_{I3}^*(\alpha',\mu)$, are sought. The corresponding fitting results are acquired respectively with additional requirements for the continuity conditions as

$$P_{I1}^*(1,\mu) = P_{I2}^*(1,\mu); P_{I2}^*(0,\mu) = P_{I3}^*(0,\mu) \tag{32}$$

The curve-fitting procedure is conducted by two steps to obtain the empirical formulas. In the first step, a limited number of values for μ are selected, and for each fixed μ, a curve fitting for P_I^* will be conducted. In the second step, the coefficients of the empirical functions attained will be further curve-fitted in terms of μ by interpolating functions such as cubic splines.

The first variable μ is assumed to be in the range of [1,50], and seven values of $\mu = 1, 2, 4, 10, 20, 35, 50$ are selected. For each μ, 200 equally spaced values of α in [0,1] and 1000 α' in [-3,1] are used to generate all the curves.

4.1 Empirical formula for Case I

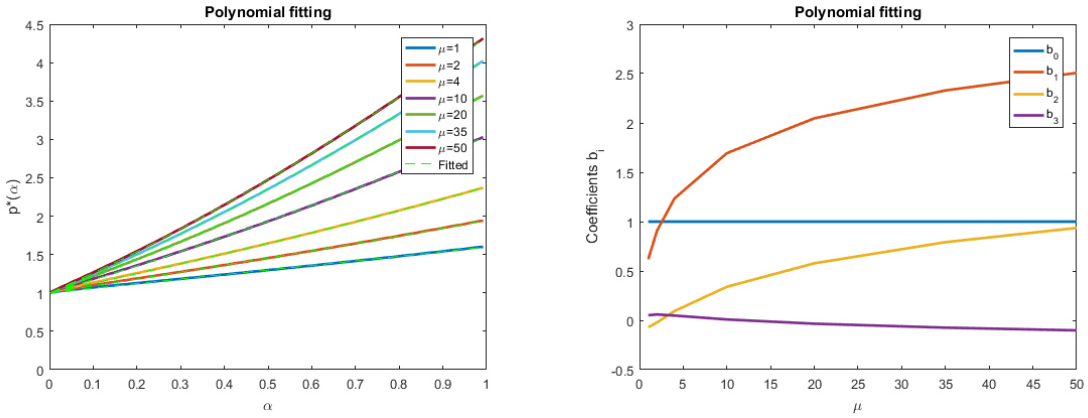

Figure 4: Case I - $0 \le \alpha \le 1$: (a) Computed P_I^* and cubic polynomial fitted curves; (b) The coefficients of the cubic polynomial

Table 2: Case I ($0 \le \alpha \le 1$): Coefficients of the cubic polynomial for different μ

coef.	μ						
	1	2	4	10	20	35	50
b_0	1.0	1.0	1.0	1.0	1.0	1.0	1.0
b_1	0.6187	0.9078	1.2343	1.6938	2.0466	2.3291	2.5069
b_2	-0.0694	-0.0220	0.0938	0.3399	0.5777	0.7919	0.9361
b_3	0.0513	0.0593	0.0481	0.0085	-0.0344	-0.0745	-0.1018
	Fitted formula						
b_0	1.0						
b_1	$0.3484\ln(\mu) + 0.6066\mu^{0.1642}$						
b_2	$0.3176\mu^{0.3782} - 0.4135$						
b_3	$-0.0745/\mu - 0.1737\mu^{0.2134} + 0.2992$						

The numerical results of P_I^* for Case I ($0 \le \alpha \le 1$) are shown in Figure 4(a) as the solid

lines. A cubic polynomial is chosen as the curve-fitted formula for $P^*_{I1}(\alpha, \mu)$

$$P^*_{I1}(\alpha, \mu) = b_0(\mu) + b_1(\mu)\alpha + b_2(\mu)\alpha^2 + b_3(\mu)\alpha^3 \tag{33}$$

which is subjected to the continuity condition (32).

The extended model reduces to the Hertz model when $\sigma = \alpha = 0$ as

$$P^*_{I1}(0, \mu) = 1 + P^*_{G1}(0, \mu) = 1 \tag{34}$$

So

$$b_0(\mu) = 1 \tag{35}$$

Four points at $\alpha = 0, 1/3, 2/3, 1$ are selected for the interpolation function $P^*_{I1}(\alpha, \mu)$. The fitted curves are plotted for each μ in Figure 4(a) by dashed lines. A very good fitting result can be observed.

The relations between four coefficients $b_i (i = 0, ..., 3)$ and μ are depicted in Figure 4(b) and listed in Table 2. A nonlinear least-squares procedure is applied to acquire the fitted formula for each coefficient with μ as presented in Table 2.

4.2 Empirical formula for Case II

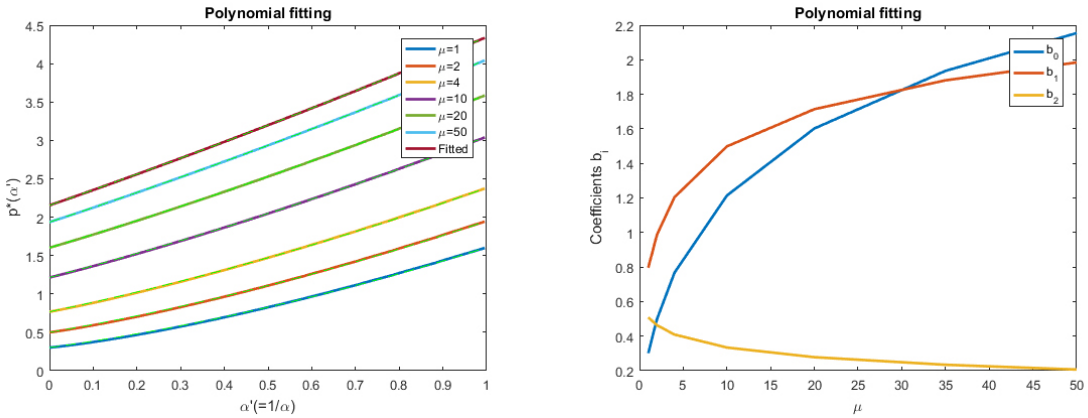

(a) (b)

Figure 5: Case II - $0 \leq \alpha' \leq 1$: (a) Computed P^*_I and quadratic polynomial fitted curves; (b) The coefficients of the quadratic polynomial

Table 3: Case II ($0 \leq \alpha' \leq 1$): Coefficients of the quadratic polynomial for different μ

coef.	μ						
	1	2	4	10	20	35	50
b_0	0.3011	0.4989	0.7672	1.2141	1.6022	1.9357	2.1544
b_1	0.7960	0.9877	1.2044	1.4986	1.7139	1.8810	1.9845
b_2	0.5082	0.4630	0.4090	0.3339	0.2781	0.2342	0.2066
	Fitted formula						
b_0	$0.2284 \ln(\mu) + 0.2786\mu^{0.3913}$						
b_1	$0.2688 \ln(\mu) + 0.7873\mu^{0.0451}$						
b_2	$-0.0778 \ln(\mu) + 0.5132\mu^{-0.0008}$						

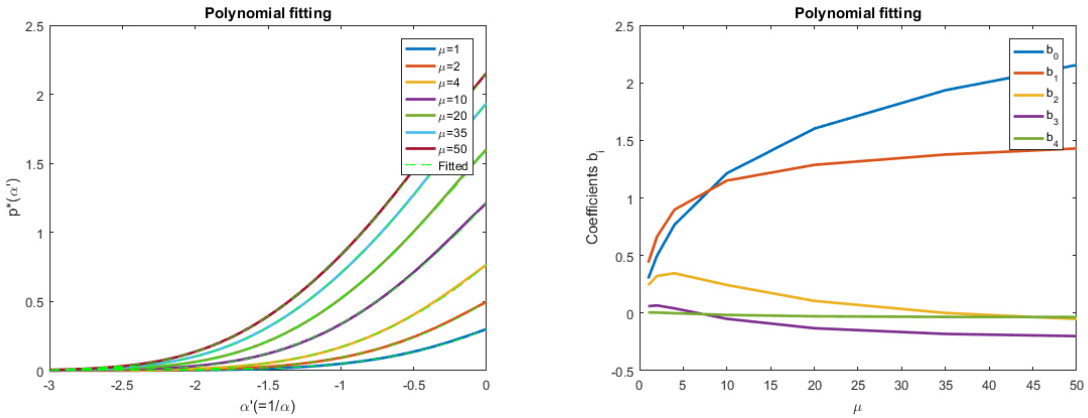

(a) (b)

Figure 6: Case III - $-3 \leq \alpha' \leq 0$: (a) Computed P_I^* and quartic polynomial fitted curves; (b) The coefficients of the quartic polynomial

Table 4: Case III ($-3 \leq \alpha' \leq 0$): Coefficients of the quartic polynomial for different μ

coef.	μ						
	1	2	4	10	20	35	50
b_0	0.3011	0.4989	0.7672	1.2141	1.6022	1.9357	2.1544
b_1	0.6187	0.6638	0.8981	1.1507	1.2872	1.3770	1.4295
b_2	0.2431	0.3227	0.3460	0.2440	0.1058	0.0012	-0.0516
b_3	0.0604	0.0665	0.0408	-0.0498	-0.1316	-0.1810	-0.1999
b_4	0.0057	0.0047	-0.0010	-0.0161	-0.0277	-0.0333	-0.0345
	Fitted formula						
b_0	$0.2284\ln(\mu) + 0.2768\mu^{0.3913}$						
b_1	$-0.2862/\mu + 0.191\ln(\mu) + 0.7095$						
b_2	$-0.5037/\mu - 0.2005\ln(\mu) + 0.7384$						
b_3	$-0.2347/\mu - 0.1473\ln(\mu) + 0.226$						
b_4	$-0.0338/\mu - 0.0245\ln(\mu) + 0.0005\mu + 0.0387$						

The numerical results of P_{I2}^* for Case II $0 \leq \alpha' \leq 1$ are showed in Figure 5(a) as the solid lines. A quadratic polynomial is chosen as the curve-fitted formula for $P_{I2}^*(\alpha', \mu)$. The continuity condition should also be satisfied in this case.

$$P_{I2}^*(\alpha', \mu) = b_0(\mu) + b_1(\mu)\alpha' + b_2(\mu)\alpha'^2 \tag{36}$$

$P_{I2}^*(\alpha', \mu)$ is determined as the interpolation function passing through the three points at $\alpha = 0, 1/2, 1$. Similar to Case I, the fitted results are presented both in Figure 5 and Table 3. It is evident that a very good fitting result has been achieved.

4.3 Empirical formula for Case III

The numerical results of P_{I3}^* for Case III $-3 \leq \alpha' \leq 0$ are showed in Figure 6(a) as the solid lines. A quartic polynomial is chosen as the curve-fitted formula for $P_{I3}^*(\alpha', \mu)$. The continuity condition should also be satisfied in this case.

$$P_{I3}^*(\alpha', \mu) = b_0(\mu) + b_1(\mu)\alpha' + b_2(\mu)\alpha'^2 + b_3(\mu)\alpha'^3 + b_4(\mu)\alpha'^4 \tag{37}$$

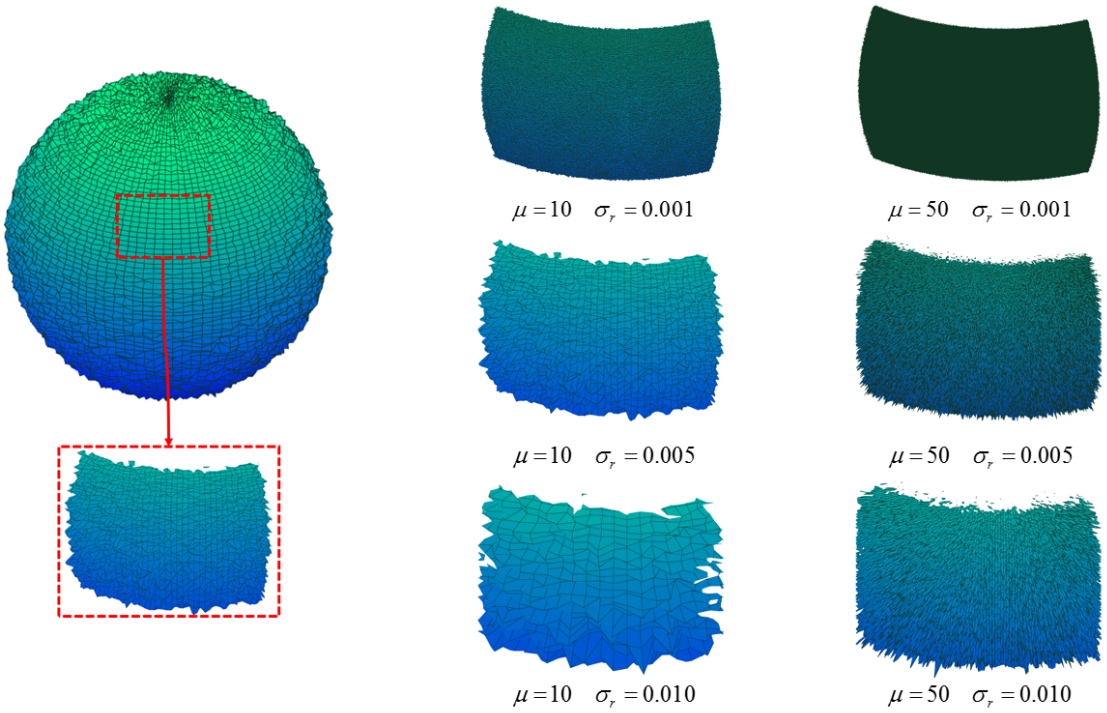

Figure 7: Rough surfaces of particles with different roughness parameters

$P^*_{I3}(\alpha', \mu)$ is determined as the interpolation function passing through the five points at $\alpha = -3, -9/4, -6/4, -3/4, 0$. Similar to the previous cases, the fitted results are presented both in Figure 6 and Table 4. It is evident that a very good fitting result has been achieved.

In summary, the final explicit form of the normal interaction law based on the extended GW model can be expressed as

$$P_I(\delta, \sigma, \mu) = \begin{cases} P_H(\delta) P^*_{I1}(\alpha, \mu); & \delta \geq \sigma \\ P_H(\sigma) P^*_{I2}(\alpha', \mu); & 0 < \delta < \sigma \\ P_H(\sigma) P^*_{I3}(\alpha', \mu); & -3\sigma < \delta < 0 \\ 0; & \delta < -3\sigma \end{cases} \tag{38}$$

5 Numerical Illustrations

The new random normal interaction law based on the extended GW model has been implemented into a DEM code to investigate the effect of surface roughness on the mechanical behaviour of a particle system. It should be noted that the material parameters used are artificially chosen, and no real surface roughness parameters are taken. The results obtained are therefore for illustration.

The material properties of the particles are: Young's modulus E=1GPa, Poisson's ratio $\nu = 0.3$, density $\rho = 2000\text{kg/m}^3$ and frictional coefficient $f = 0.2$. A constant frictional coefficient is chosen here to exclusively show the influence of the roughness parameters, although the coefficient itself is entirely determined by these parameters.

Four levels of surface roughness ratios $\sigma_r = (0, 0.001, 0.005, 0.01)$ are considered for the following simulations, where $\sigma_r = 0$ represents the smooth surface. The surface roughness σ of a particle is set to be proportional to its radius r: $\sigma = \sigma_r r$. The second roughness parameter μ is taken to be 10 or 50. The first roughness parameter σ can be regarded as the measure-

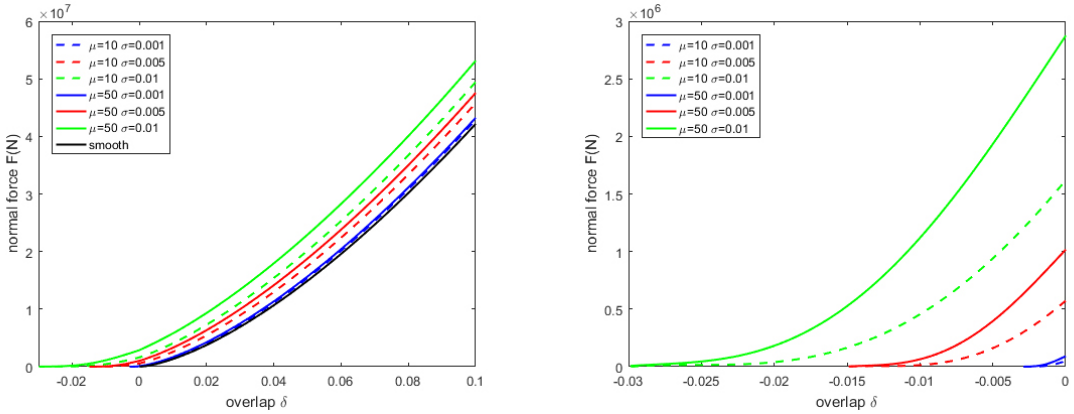

Figure 8: The normal force interaction laws for particles with different surface roughness parameters

ment of surface roughness in the normal direction which represents the height of the asperity. The second roughness parameter may be viewed as the measurement of surface roughness in the tangent direction in relation to the number and the radii of curvature of the asperities. The surface of rough particles ($r = 1$) with different roughness parameters are depicted in Figure 7.

In summary, seven samples with different roughness parameters have been created. The normal contact laws for a unit particle ($r = 1$) with different surface roughness parameters are showed in Figure 8(a), with an enlarged view in Figure 8(b) for overlap $\delta < 0$. It is obvious that as σ_r and μ increase, the value and range of the normal force increase as well. Unlike the linear or Hertz contact law which defines the relationship between the total force and the overlap by a power function with a constant exponent of 1 or 1.5.

The current normal contact law considers different contact behaviour of rough particles at different contact stages. At the initial stage of contact between two rough particles, only some asperities are in contact which corresponds to the slow growth part (Case III) of the random normal contact law. As the overlap increases from zero, the contact force between rough particles is subject to a rapid growth (Cases I and II). The random normal contact law can reflect the contact behaviour between rough particles more reasonably.

Compressive tests will be simulated below to illustrate the effect of surface roughness on the macro and micro mechanical characteristics of a particle assembly. The particle assembly is generated randomly in a cubic box of the side length 60cm. The particle diameters obey the Gaussian distribution with the average radius of 1cm and the relative deviation of 0.25. The total number of the particles is 14812.

Two compressive loadings are carried out on the sample: one-dimensional compression and three-dimensional compression. For the one-dimensional compress test, the sample is first compacted to reach an initial isotropic stress of 0.5MPa. By setting the top and bottom boundaries as rigid wall, and the periodic boundary to the two lateral directions, the one-dimensional compression is simulated by moving the top and bottom walls at a constant velocity in the vertical direction (Figure 9(a)). For the three-dimensional compress test, the initial isotropic stress is 5MPa. The sample is enclosed with rigid walls in all directions. Three-dimensional compression is simulated by moving the top and bottom walls at the same constant velocity and using a servo-control mechanism to maintain the stress on the lateral walls as 5MPa (Figure 9(b)).

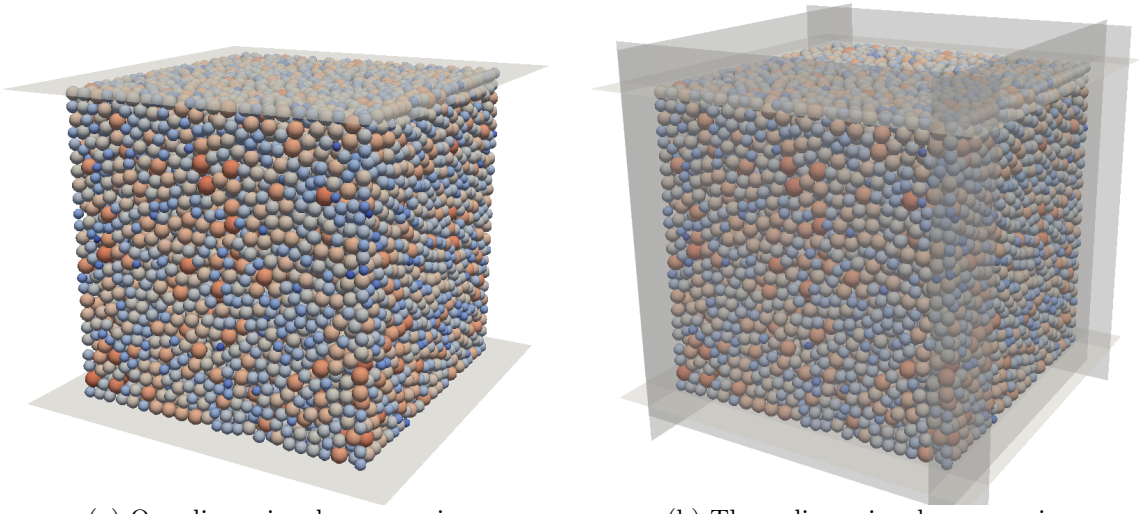

(a) One-dimensional compression (b) Three-dimensional compression

Figure 9: Numerical samples

5.1 One-dimensional compression

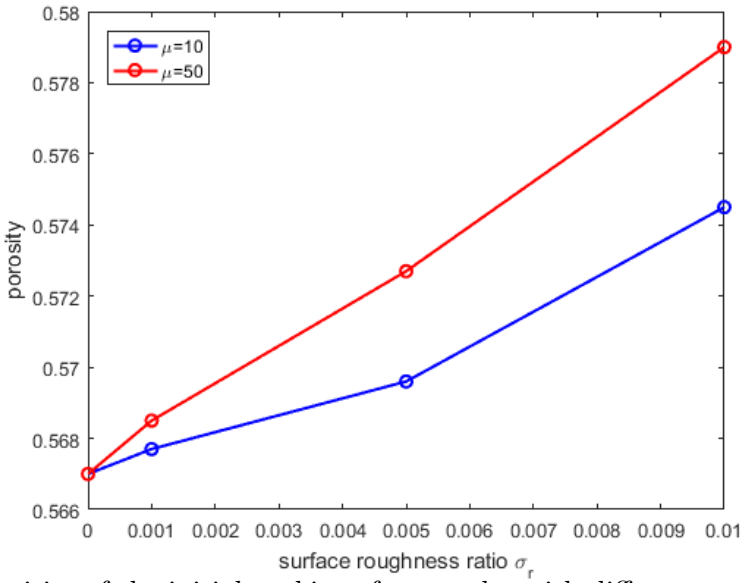

Figure 10: Porosities of the initial packings for samples with different roughness parameters

The initial porosities of samples with different roughness parameters with an isotropic stress state of 0.5MPa are displayed in Figure 10. It shows that as the surface roughness ratio σ_r increases, the porosity almost linearly increases from 0.5670 to 0.5745 ($\mu = 10$) or 0.5790 ($\mu = 50$). A larger roughness parameter μ leads to a higher porosity which indicates that surface roughness makes the initial packing looser. This phenomenon can be explained by investigating the normal contacts between particles.

Figure 11 depicts the normal contact links between particles. As mentioned above, the random normal contact law is divided into three cases: Case I: $\sigma \leq \delta$; Case II: $0 \leq \delta < \sigma$; Case III: $-3\sigma \leq \delta < 0$. In Figure 11, the contact belonging to Case I is in red, Case II in yellow and Case III in blue. It can be seen that increasing surface roughness parameters gradually increases the number of contacts in Cases II and III.

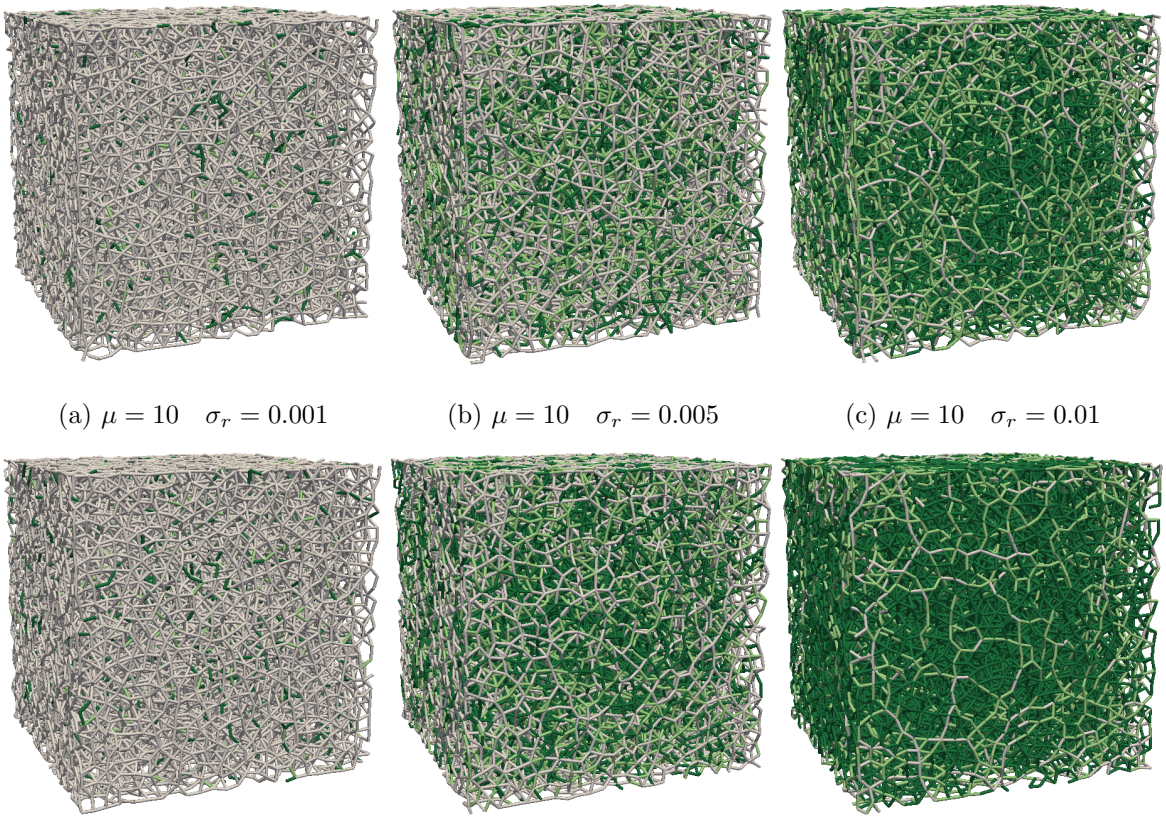

(a) $\mu = 10 \quad \sigma_r = 0.001$ (b) $\mu = 10 \quad \sigma_r = 0.005$ (c) $\mu = 10 \quad \sigma_r = 0.01$

(d) $\mu = 50 \quad \sigma_r = 0.001$ (e) $\mu = 50 \quad \sigma_r = 0.005$ (f) $\mu = 50 \quad \sigma_r = 0.01$

Figure 11: Normal contact links for initial packing samples with different roughness parameters

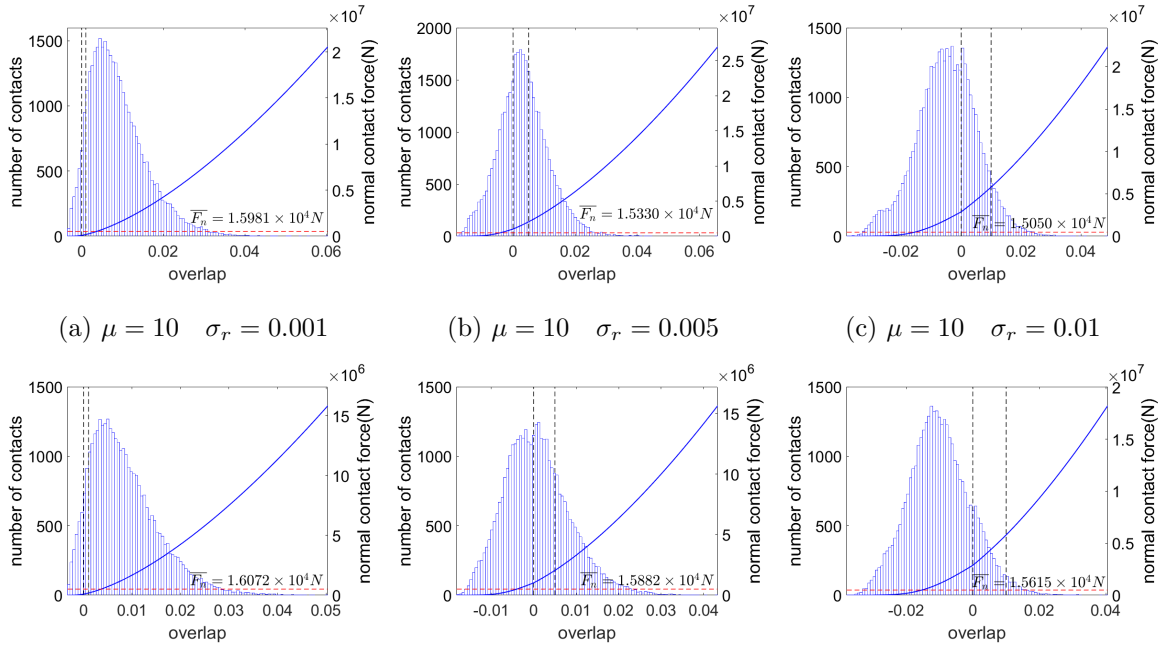

(a) $\mu = 10 \quad \sigma_r = 0.001$ (b) $\mu = 10 \quad \sigma_r = 0.005$ (c) $\mu = 10 \quad \sigma_r = 0.01$

(d) $\mu = 50 \quad \sigma_r = 0.001$ (e) $\mu = 50 \quad \sigma_r = 0.005$ (f) $\mu = 50 \quad \sigma_r = 0.01$

Figure 12: Normal contact distributions and contact laws for different samples

Table 5: Percentage of the number of contacts number of initial packings (One-dimensional compression)

	$\mu = 10$			$\mu = 50$		
Case	$\sigma_r = 0.001$	$\sigma_r = 0.005$	$\sigma_r = 0.01$	$\sigma_r = 0.001$	$\sigma_r = 0.005$	$\sigma_r = 0.01$
I	91.07%	38.29%	6.58%	88.63%	26.54%	2.25%
II	3.94%	28.33%	25.93%	4.59%	25.09%	12.42%
III	4.99%	33.38%	67.49%	6.78%	48.37%	85.33%

Table 5 lists the percentage of the number of contacts in each case for six samples with rough particles. Obviously, all the contacts in the samples of smooth particles belong to Case I as the random normal contact law reduces to the Hertz contact law. The two roughness parameters σ_r and μ affect the percentage to different degrees. σ_r determines the ranges of the three cases so has a more significant influence. For both $\mu = 10$ and $\mu = 50$, as σ_r increases from 0.001 to 0.01, the percentage of the number of contacts in Case I decreases from around 90% to less than 10%. The percentage in Case II firstly increases then decreases as σ_r increases from 0.001 to 0.05, then to 0.01. Meanwhile, the percentage in Case III generally increases. For all σ_r=0.001,0.05,0.01, increasing μ increases the percentage in Case III while decreases the percentage in Cases I and II.

Figure 12 illustrates the normal contact distribution, average normal contact force and contact force vs the overlap for different samples. The blue solid line represents the normal contact force vs overlap, the dashed red line represents the average normal force, the dashed vertical black lines divide the contacts into the three cases, and the blue histogram indicates the normal contact distribution over the overlap range. As the initial state stress for the six samples is the same, the average normal force is in the range of $1.5 \sim 1.6 \times 10^4$N. With the increase of σ_r, the average normal force decreases because the extension of the contact range leads to more normal contacts but with small values. The intersection of the average normal force and the normal contact law (red dashed line and blue solid line) determines the overlap where most contacts occur. When $\sigma_r = 0.001$, for both μ, this intersection is located within Case I, and most of the contacts occur in Case I as well. When $\sigma_r = 0.005$, for $\mu = 10$, the intersection is near the line dividing Cases II and III; the contacts in Case II (28.33%) and Case III (33.38%) are almost the same. While for $\mu = 50$, the intersection is in Case III, making the percentage of contacts in Case III (48.37%) two times of it in Case II (25.09%). When $\sigma_r = 0.01$, the intersection is in Case III and most contacts occur in Case III.

The one-dimensional compression is preformed on each sample reaching the final axial strain of 0.2. Figure 13 shows the compression results for seven samples. It can be seen from Figure 13(b) that the sample with smooth particles has the smallest coordination number. Increasing σ_r will increase the coordination number while increasing μ has the opposite effect. The coordination number increases as the porosity of the sample decreases or the contact range of the normal contact law extends. The contact range is enlarged with the increase of σ_r (Figure 8). The porosity of the sample increases with the increase of μ (Figure 10). Figure 13(a) shows the stress-strain curves, and the zoomed details of the stress-strain curves are shown in Figure 14 for three axial strains (0.1,0.15 and 0.2), together with the corresponding contacts distributions.

The compression stress exhibits a complicated relation with σ_r and μ. It can be explained by collectively considering the coordination number, the normal contact distribution and the normal contact law. Contacts between particles decide the stress state of the sample.

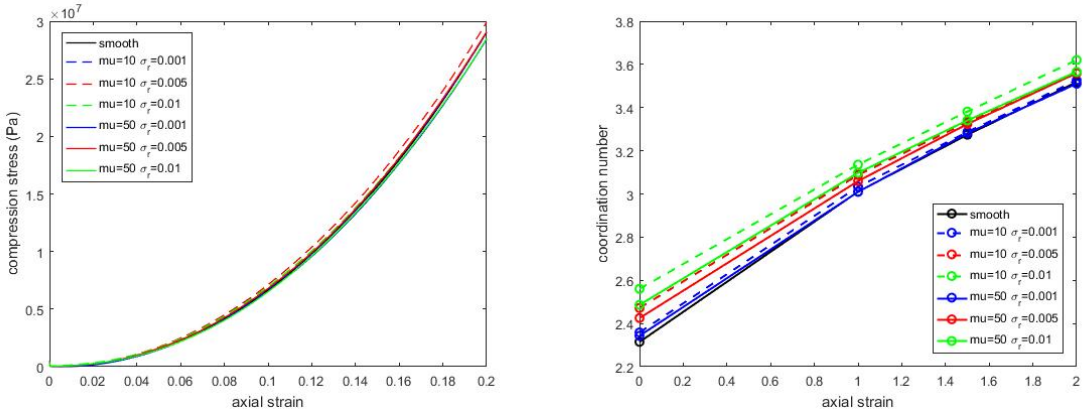

(a) Stress-strain curves (b) Coordination number

Figure 13: Results of seven different samples under one-dimensional compression

Both the number of contacts and the corresponding forces make contributions. As roughness parameters increase, the ranges for Cases II and III become larger.

Figure 14(a) illustrates the stress state when the axial strain is 0.1, while the left figure is an enlarged view of Figure 13 for the axial strain between 0.09 and 0.1. For $\mu = 10$, $\sigma_r = 0.005$ produces the largest stress and $\sigma_r = 0.001$ leads to the smallest stress. This is because increasing σ_r will extend the contact range which will increase the number of contacts in Case III. A larger contact number will result in the increase of stress as shown by comparison between $\sigma_r = 0.005$ and $\sigma = 0.001$. While the contact force in Case III is very small especially for large σ_r, if the increase of contact number cannot offset the decrease of the normal contact force, the stress will decrease by comparison between $\sigma_r = 0.005$ and $\sigma = 0.01$. For each σ_r, the stress for $\mu = 10$ is larger than that for $\mu = 50$. This is because that the total contact number is smaller for $\mu = 50$ due to a looser packing.

In Figures 14(b) and (c), where the axial strains are 0.15 and 0.2 respectively, the difference between the stress for $\sigma_r = 0.001$ and $\sigma_r = 0.01$ diminishes gradually. For $\sigma_r = 0.01$, the stress increase is caused by more contacts in Cases I and II and fewer contacts in Case III during the compression (see Figure 15). For $\sigma_r = 0.001$, small contact ranges of Cases II and III means that most of the contacts belong to Case I. The stress of $\sigma_r = 0.005$ is the largest. Compared to $\sigma_r = 0.01$, smaller ranges of Cases II and III for $\sigma_r = 0.005$ make more contacts occurring in Case I with larger normal forces. Compared to $\sigma_r = 0.001$, the larger ranges of Case II and III for $\sigma_r = 0.005$ gives rise to a larger contact number.

In summary, surface roughness makes the initial packing of the samples more looser. When the particle assembly is under one-dimensional compression, the sample of particles with moderate roughness parameters shows a higher strength.

5.2 Three-dimensional compression

The initial isotropic stress state for the three-dimensional compression is 5MPa which is ten times of that for the one-dimensional compression. Different contacts distributions can be observed from these initial packings.

Table 6 lists the percentage of the number of contacts in each case for all the samples of rough particles. For the smooth surface when $\sigma_r = 0$, all the contacts belong to Case I. For all the rough samples, the percentage in Case I is dominant. Under the isotropic stress of 5MPa,

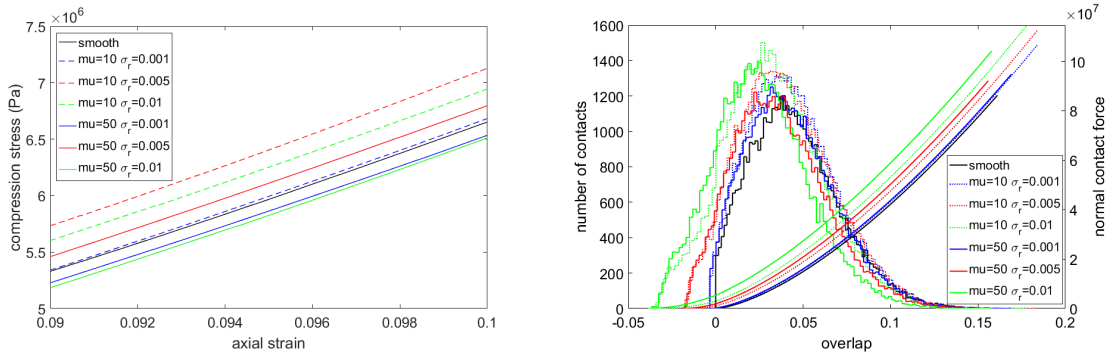

(a) Axial strain=0.1

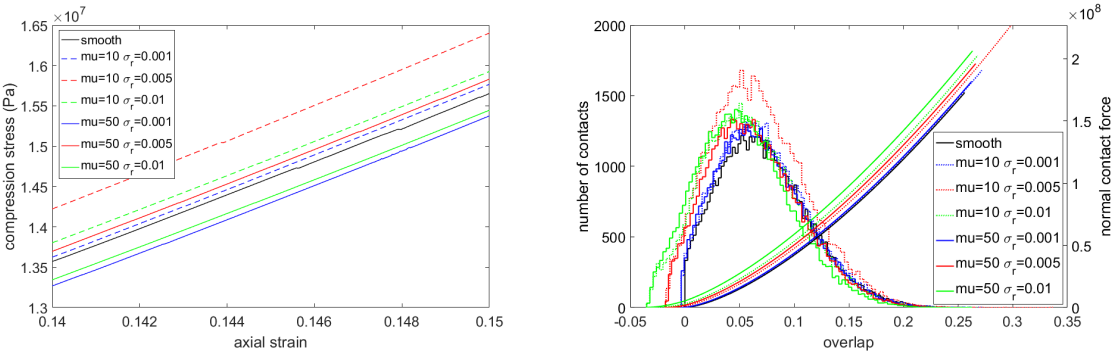

(b) Axial strain=0.15

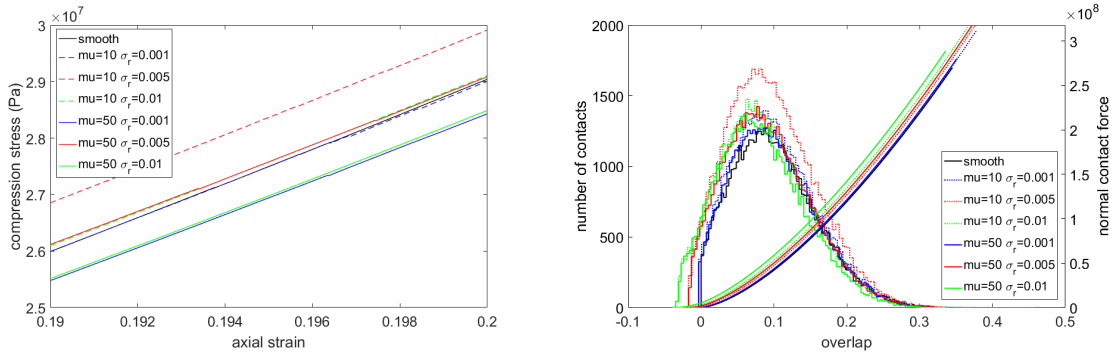

(c) Axial strain=0.2

Figure 14: Stress-strain curves and corresponding normal contact distribution

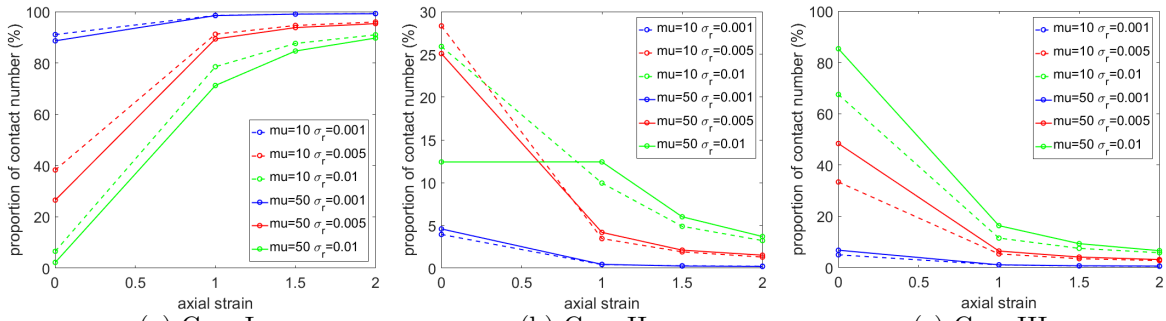

(a) Case I (b) Case II (c) Case III

Figure 15: Relation between percentage of the number of contacts and axial strain for three cases

the packing is denser than the initial packing under the stress of 0.5MPa. More contacts are shifted to Case I.

Table 6: Percentage of the number of contacts of initial packings (Three-dimensional compression)

	$\mu = 10$			$\mu = 50$		
Case	$\sigma_r = 0.001$	$\sigma_r = 0.005$	$\sigma_r = 0.01$	$\sigma_r = 0.001$	$\sigma_r = 0.005$	$\sigma_r = 0.01$
I	99.0%	93.75%	84.21%	98.82%	92.38%	76.39%
II	0.33%	2.42 %	8.32 %	0.28%	3.08 %	11.76%
III	0.67%	3.83 %	7.47 %	0.90%	4.54 %	11.85%

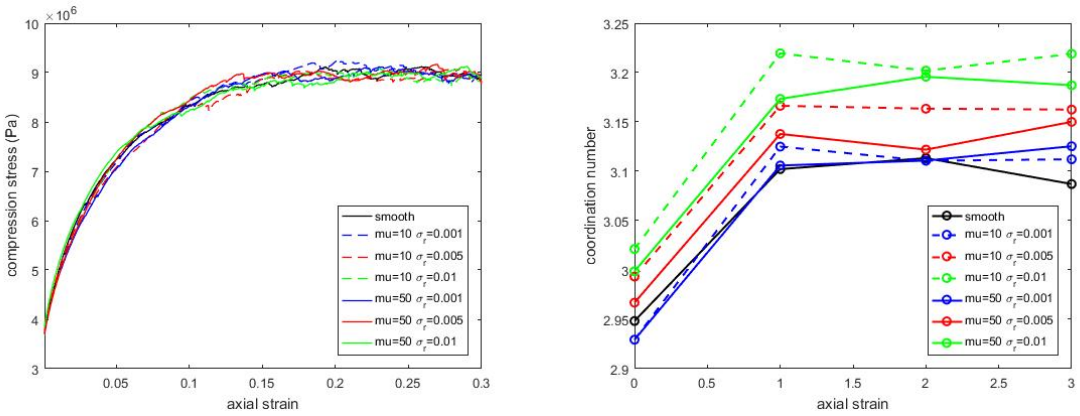

(a) Stress-strain curves (b) Coordination number

Figure 16: Results of seven different samples under three-dimensional compression

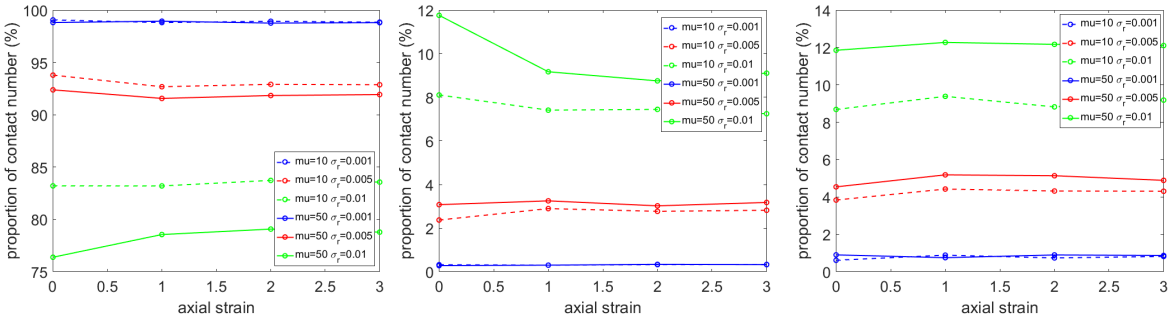

(a) Case I (b) Case II (c) Case III

Figure 17: Relation between percentage of the number of contacts and axial strain for three cases

The three-dimensional compression is performed on each sample reaching the final axial strain of 0.3. Figure 16 shows the stress-strain curves and corresponding variations of coordination number for seven samples. As the influence of roughness parameters is significant in the initial stage of the contact (Case III), the difference of the mechanical response between different samples is not obvious compared to the difference in the one-dimensional compression with the initial isotropic stress of 0.5MPa. Two reasons result in this phenomenon. Firstly, as shown in Table 6, the large isotropic stress leads to almost the same contact distribution for different initial packings. Secondly, during the compression, the lateral compression stress is kept to be 5MPa which maintains a dense compaction of the sample. Under such a condition,

the percentages of the number of contacts for the three contact cases keep constantly during the compression process for all the samples as shown in Figure 17.

In summary, the roughness parameters have a significant influence on the looser packed samples with more contacts occurring in the initial contact stage. For the dense packing, the deformation of the particles is sufficiently large which makes the influence of the surface roughness negligible.

Overall, compared to other properties of particles such as Youngs modulus, Poissons ratio and density, the asperity characteristics play a secondary role in the macro property of the particle systems. This is the main reason that the Hertz model governs the macro stress/strain curves. The influence of the surface roughness cannot be neglected, however, especially for a loosely packed particle system. The influence caused by the roughness characteristics on the packing under an initial isotropic stress of 0.5MPa is more significant than on the packing under the initial isotropic stress of 5MPa. For both particle systems considered, the discrepancies caused by the roughness are more significant at the initial compressive loading stage.

6 Concluding Remarks

A random normal contact law based on the extended GW model for spheres with surface roughness has been developed in this work. With the two non-dimensional forms proposed, only two roughness parameters are required. The contact forces against different roughness parameters are obtained numerically and then curve-fitted to derive an empirical formula as a new and improved normal interaction law for spheres with surface roughness. The resulting normal contact law has been incorporated into the existing DEM modelling procedure to conduct compression tests under different loading paths. Numerical simulations illustrate the influence of roughness parameters on the mechanical behaviour of the particle system. The results show that surface roughness makes the initial packing of a sample more looser and has a greater influence on looser packed samples as expected. It also shows that an assembly of particles with moderate roughness parameters may exhibit a higher strength. It is also possible to extend the current work to drive both a tangential frictional model and a possible rolling resistant model, and the related work will be reported later.

It should be highlighted again that the current developed contact law is essentially based on the classic GW theory where asperities are assumed to deform elastically. When the overlap is large, some asperities, particularly those with large heights, will deform inelastically or plastically. Therefore, the proposed contact law is more appropriate for small overlap cases and/or for materials likely behaving elastically. Nevertheless, plastic-based GW models can be readily incorporated within the current framework. Further developments to relax other conditions inherent in the GW theory are also worth pursuing.

It is also important to mention that the current contact model has not been verified by any experiment which is beyond the scope of the current work. This is mainly due to the fact that very few experimental investigations of normal contact laws for rough surfaces have been reported. In the limited cases, the experiments mainly focus on the contact between two rough flat surfaces [33, 34, 35, 36], and most results lack the information that can be used to validate theoretical models. Therefore more work is clearly needed in this aspect. Due to the lack of real parameters of particle roughness and related experiment results, it is not easy to clarify the application domain of the proposed model yet.

References

[1] Cundall, P.A. and Strack, O.D. A discrete numerical model for granular assemblies. *Geotechnique.* 29(1):47-65, 1979.

[2] Feng, Y.T., Zhao, T., Kato, J. and Zhou, W. Towards stochastic discrete element modelling of spherical particles with surface roughness: A normal interaction law. *Computer Methods in Applied Mechanics and Engineering.* 315: 247-272, 2017.

[3] Cho, N.A., Martin, C.D. and Sego, D.C. A clumped particle model for rock. *International Journal of Rock Mechanics and Mining Sciences.* 44(7): 997-1010, 2007.

[4] Hryciw, R.D., Zheng, J. and Shetler, K. Particle roundness and sphericity from images of assemblies by chart estimates and computer methods. *Journal of Geotechnical and Geoenvironmental Engineering.* 142(9): 04016038, 2016.

[5] Jensen, R.P., Bosscher, P.J., Plesha, M.E. and Edil, T.B. DEM simulation of granular mediastructure interface: effects of surface roughness and particle shape *International Journal for Numerical and Analytical Methods in Geomechanics.* 23(6):531-547, 1999.

[6] Wang, L., Park, J.Y. and Fu, Y. Representation of real particles for DEM simulation using X-ray tomography. *Construction and Building Materials.* 21(2): 338-346, 2007

[7] Lu, M. and McDowell, G.R. The importance of modelling ballast particle shape in the discrete element method. *Granular matter.* 9(1-2): 69, 2007

[8] Ferellec, J.F. and McDowell, G.R. A simple method to create complex particle shapes for DEM. *Geomechanics and Geoengineering: An International Journal.* 3(3): 211-216, 2008

[9] Shamsi, M.M. and Mirghasemi, A.A. Numerical simulation of 3D semi-real-shaped granular particle assembly. *Powder technology.* 28(2): 431-446, 2012

[10] Iwashita, K. and Oda, M. Rolling resistance at contacts in simulation of shear band development by DEM. *Journal of engineering mechanics.* 124(3): 285-292, 1998

[11] Garcia, X., Latham, J.P., Xiang, J.S. and Harrison, J.P. A clustered overlapping sphere algorithm to represent real particles in discrete element modelling. *Geotechnique.* 59(9): 779-784, 2009.

[12] Zhou, W., Ma, G., Chang, X.L. and Duan, Y. Discrete modeling of rockfill materials considering the irregular shaped particles and their crushability. *Engineering Computations.* 32(4):1104-1120, 2015.

[13] Feng, Y.T., and Owen, D. R. J. A 2D polygon/polygon contact model: algorithmic aspects. *Engineering Computations.* 21: 265-277, 2004

[14] Han, K., Feng, Y.T., and Owen, D. R. J. Polygon-based contact resolution for superquadrics. *International Journal for Numerical Methods in Engineering.* 66: 485501.2006

[15] Feng, Y.T., Han, K., and Owen, D. R. J. Energy-conserving contact interaction models for arbitrarily shaped discrete elements. *Computer Methods in Applied Mechanics and Engineering.* 205-208: 169-177, 2012

[16] Feng, Y.T., Han, K., and Owen, D. R. J. A generic contact detection framework for cylindrical particles in discrete element modelling. *Computer Methods in Applied Mechanics and Engineering.* 315: 632-651, 2017

[17] Jiang, M.J., Yu, H.S. and Harris, D. A novel discrete model for granular material incorporating rolling resistance. *Computers and Geotechnics.* 32(5): 340-357, 2005

[18] Huang, X., Hanley, K.J., OSullivan, C. and Kwok, C.Y. Implementation of rotational resistance models: a critical appraisal. *Particuology.* 34: 14-23, 2017

[19] Jiang, M.J., Leroueil, S., Zhu, H., Yu, H.S. and Konrad, J.M. Two-dimensional discrete element theory for rough particles. *International Journal of Geomechanics.* 9(1): 20-33, 2009

[20] Wilson, R., Dini, D. and Van Wachem, B. The influence of surface roughness and adhesion on particle rolling. *Powder Technology.* 312: 321-333, 2017

[21] Greenwood, J.A. and Williamson, J.P. Contact of nominally flat surfaces. *Proceedings of the Royal Society of London A: Mathematical, Physical and Engineering Sciences.* 295(1442): 300-319, 1966

[22] Beheshti, A. and Khonsari, M.M. On the contact of curved rough surfaces: contact behavior and predictive formulas. *Journal of Applied Mechanics.* 81(11): 111004, 2014

[23] Feng Y. T. and Zhao T. An Extended Greenwood-Williamson Model for Rough Spheres. *Journal of Applied Mechanics.* 2018 (to appear)

[24] Greenwood, J.A. and Tripp, J.H. The elastic contact of rough spheres. *Journal of Applied Mechanics.* 34(1): 153-159, 1967

[25] Beheshti, A. and Khonsari, M.M. Asperity micro-contact models as applied to the deformation of rough line contact. *Tribology International.* 52: 61-74, 2012

[26] Nayak, P.R. Random process model of rough surfaces. *Journal of Lubrication Technology.* 93(3): 398-407, 1971

[27] McCool, J.I. Comparison of models for the contact of rough surfaces. *Wear.* 107(1): 37-60, 1986

[28] Johnson, K.L. Contact Mechanics, Cambridge University Press, Cambridge, 1985.

[29] Pullen, J. and Williamson, J.B.P On the plastic contact of rough surfaces. *Proceedings of the Royal Society A.* 327(1569): 159-173, 1972

[30] Chang, WR., Etsion, I. and Bogy, D BASME An elastic-plastic model for the contact of rough surfaces. *Journal of tribology.* 109: 257-263, 1987

[31] Zhao, Y., Maietta, D.M. and Chang, L. An asperity microcontact model incorporating the transition from elastic deformation to fully plastic flow. *Journal of Tribology.* 122(1): 86-93, 2000

[32] Jackson, Robert L and Green, Itzhak A statistical model of elasto-plastic asperity contact between rough surfaces. *Tribology International.* 39: 906-914, 2006

[33] Yamada, K., Takeda, N., Kagami, J. and Naoi, T. Mechanisms of elastic contact and friction between rough surfaces. *Wear.* 48(1): 15-34, 1978

[34] Yoshioka, N. and Scholz, C.H. Elastic properties of contacting surfaces under normal and shear loads: 2. Comparison of theory with experiment. *Journal of Geophysical Research: Solid Earth.* 94(B12): 17691-17700, 1989

[35] Berthe, L., Sainsot, P., Lubrecht, A.A. and Baietto, M.C. Plastic deformation of rough rolling contact: An experimental and numerical investigation. *Wear.* 312(1-2): 51-57, 2014

[36] Garca, J.M. and Martini, A. Measured and Predicted Static Friction for Real Rough Surfaces in Point Contact. *Journal of Tribology.* 134(3): 031501, 2012